Materials Horizons

ROYAL SOCIETY OF CHEMISTRY

COMMUNICATION

View Article Online
View Journal

Cite this: DOI: 10.1039/d5mh01066g

Received 5th June 2025,
Accepted 7th August 2025

DOI: 10.1039/d5mh01066g

rsc.li/materials-horizons

Bionic fire-resistant chitosan aerogels with the triple stealth functionality: microwaves, infrared and sound

Xiuhong Sun,[a] Jinhu Hu,[a] Jin Cao,[a] Lei Chen,[f] Tinglu Song,[g] Xing Su,[h] Pingan Song,[de] Yang Li,[i] Shengchao Huang,[j] Ye-Tang Pan,*[ak] Mingliang Ma*[c] and Congling Shi[b]

The complex electromagnetic environment in national defense requires tailored microwave-absorbing materials for different scenarios. In aerospace, lightweight and multifunctional materials are especially important. While aerogels offer low density, they must be further modified to become effective microwave absorbers. Traditional fillers like carbon nanotubes often cause problems such as impedance mismatch, particle aggregation, and poor chemical reactivity, limiting their performance in aerogel systems. To overcome these issues, we used an electrostatic self-assembly strategy to deposit a FeCo-based metal–organic framework (MOF) onto black phosphorus nanosheets (BPNSs). The resulting BPNS@MOF was then integrated into a chitosan-derived aerogel through Schiff base reactions between the amino groups of the MOF and the aldehyde groups of glutaraldehyde. After freeze-drying and high-temperature pyrolysis, we obtained a lightweight, multifunctional carbon/BPNS@MOF aerogel (CS-2). CS-2 exhibits excellent electromagnetic properties, with a minimum reflection loss of −72.13 dB and an effective absorption bandwidth of 5.88 GHz. Radar cross-section simulations confirm its stealth potential. In addition, CS-2 shows ultralow thermal conductivity (0.05 W (m K)$^{-1}$), superior fire resistance, and outstanding sound absorption performance (a 5.0 mm-thick sample achieves a sound absorption coefficient of above 0.95). These features demonstrate its strong potential for multifunctional aerospace and defense applications.

New concepts

In this study, we pioneered the use of magnetic metal–organic frameworks to modify black phosphorus nanosheets, successfully fabricating a chitosan-derived carbon aerogel multifunctional material that integrates excellent microwave absorption, sound absorption, thermal insulation, and fire resistance. Remarkably, at a thickness of approximately 3.0 mm, the material achieves a reflection loss (RL) value below −72 dB, positioning it among the most promising candidates for practical multifunctional microwave absorbing materials. While microwave absorbers have been extensively studied, the application of black phosphorus nanosheets in this field remains largely unexplored, particularly in the context of hybridizing MOFs with BPNSs to fabricate lightweight, multifunctional materials. This work demonstrates the effectiveness of MOF-modified BPNSs in enhancing the microwave absorption properties of carbonized aerogels and, more importantly, highlights the versatility of the resulting material. Given its unique combination of lightweight structure and integrated functionalities, this aerogel exhibits great potential for application in aerospace platforms, such as aircraft and spacecraft, where multifunctionality and weight reduction are crucial.

1. Introduction

With the rapid advancement of modern technology, microwave technology has found widespread applications in both military and civilian sectors.[1,2] However, the diverse operational environments impose distinct and stringent requirements on microwave-absorbing materials.[3,4] For instance, in marine

[a] National Engineering Research Center of Flame Retardant Materials, School of Materials Science & Engineering, Beijing Institute of Technology, Beijing 100081, P. R. China. E-mail: pyt@bit.edu.cn
[b] Beijing Key Laboratory of Metro Fire and Passenger Transportation Safety, China Academy of Safety Science and Technology, Beijing 100012, China
[c] School of Civil Engineering, Qingdao University of Technology, Qingdao, 266520, Shandong, China. E-mail: mamingliang@qut.edu.cn
[d] Centre for Future Materials, University of Southern Queensland, Springfield Central, QLD, 4300, Australia
[e] School of Agriculture and Environmental Science, University of Southern Queensland, Springfield, QLD, 4300, Australia
[f] China University of Mining and Technology, Beijing, Xueyuan Road, Haidian District, Beijing 100083, China
[g] Experimental Center of Advanced Materials, School of Materials Science and Engineering, Beijing Institute of Technology, Beijing 100081, China
[h] School of Materials Science and Engineering, Beijing Institute of Technology, Beijing, 100871, China
[i] National Engineering Research Center for Rubber and Plastic Moulds, Zhengzhou University, Zhengzhou 450001, Henan, China
[j] Hubei Three Gorges Laboratory, No. 1, Mazongling Road, Xiaoting District, Yichang City, Hubei Province, China
[k] Tangshan Institute, School of Materials Science & Engineering, Beijing Institute of Technology, Tangshan 063000, Hebei, China

environments, corrosion-induced coating degradation often leads to the failure of microwave-absorbing performance in naval vessels and submarines, highlighting the critical need for developing corrosion-resistant microwave absorbers.[5] In contrast, for portable electronic devices, aircraft, and spacecraft, lightweight and multifunctional microwave-absorbing materials are of paramount importance to meet the stringent demands of weight reduction and performance integration.[6] In recent years, aerogels have attracted considerable attention as promising candidates for advanced functional materials due to their unique nanoscale architecture, characterized by ultrahigh porosity and extremely low density.[7] Their highly open three-dimensional network structure enables effective regulation of various physical fields, including thermal, acoustic, and electromagnetic waves, thereby offering significant potential for the development of lightweight and multifunctional materials tailored for specific application scenarios.[8–10]

Among the various aerogel systems, chitosan (CS) aerogels stand out as a class of three-dimensional porous materials derived from the sol–gel transition and drying processes of natural polysaccharide chitosan.[11–13] Notably, chitosan possesses a high theoretical carbon content (approximately 44.7–47%) and abundant nitrogen functionalities, making it an excellent precursor for the preparation of nitrogen-doped porous carbon materials with inherent electrical conductivity after pyrolysis. Furthermore, the unique three-dimensional porous architecture of aerogels facilitates multiple reflection and scattering pathways for incident electromagnetic waves, thereby extending the wave propagation time within the material and enhancing energy dissipation.[14] However, carbon materials obtained solely through the carbonization of chitosan often suffer from inherent limitations, including insufficient dielectric loss, a single loss mechanism, and poor impedance matching, which hinder their practical applications in high-performance microwave absorption.[15] Consequently, a key research focus has been the development of strategies to preserve the porous framework of chitosan aerogels during high-temperature carbonization while simultaneously enhancing dielectric loss and introducing multiple synergistic loss mechanisms.[16,17]

Unfortunately, although traditional carbon-based materials such as carbon nanotubes (CNTs) and graphene exhibit excellent electrical conductivity, their excessively high conductivity often leads to severe impedance mismatch, thereby limiting the effective coupling and absorption of microwave energy.[18,19] Moreover, their strong hydrophobicity and chemical inertness tend to cause aggregation in composite systems. Conventional strategies to improve their dispersion, such as strong acid etching or plasma treatments, can damage their intrinsic sp^2-hybridized structures, ultimately degrading their functional performance.[20] In contrast, black phosphorus nanosheets (BPNSs), as an emerging two-dimensional (2D) material, offer a more balanced set of properties, including moderate electrical conductivity and high surface chemical reactivity.[21–23] Its tunable bandgap and high carrier mobility enables precise control over carrier concentration and dielectric response, thereby achieving an optimized balance between dielectric loss and impedance matching. This dual advantage facilitates the reduction of electromagnetic wave reflection while enhancing internal energy dissipation. Additionally, the layered structure of BPNSs, with its abundant interfaces, defects, and edge states, contributes to significant interfacial polarization effects under an alternating electromagnetic field, thereby promoting efficient energy dissipation and further enhancing microwave absorption performance.[24] For example, Wang *et al.* reported that by tuning the ratio of tellurium-doped black phosphorus (Te-BP) to carbonyl iron, they successfully modulated the dielectric dispersion and impedance characteristics of lightweight and porous Te-BP/aramid nanofiber/carbonyl iron powder aerogels (TBAC). As a result, the optimized aerogel demonstrated exceptional microwave absorption performance, with a broad effective absorption bandwidth (8.46 GHz at −35 dB for a 1.9 mm-thick sample) and an ultralow density (0.02–0.043 g cm^{-3}).[25]

Nevertheless, intrinsic black phosphorus nanosheets (BPNSs) are a non-magnetic material that lacks magnetic loss mechanisms. As a result, it cannot effectively induce natural resonance or eddy current loss, which are critical for magnetic energy dissipation in microwave frequency ranges. This limitation significantly hampers the realization of synergistic electromagnetic absorption and restricts the development of broadband, high-efficiency microwave absorption materials. Moreover, BPNSs exhibit extreme sensitivity to environmental conditions and are prone to rapid oxidation and degradation when exposed to air, leading to irreversible structural collapse and performance deterioration.[26–28] Surface passivation of BPNSs using magnetic materials through coordination strategies has emerged as an effective approach to address these challenges.[29] Notably, BPNSs possess a puckered honeycomb lattice in which each phosphorus atom forms covalent bonds with three neighboring phosphorus atoms, leaving one lone pair of electrons exposed. By coordinating these lone pair electrons with other elements, it is possible to prevent undesirable P–O interactions, thereby mitigating BPNS oxidation.[30] For instance, Zhao *et al.* successfully employed titanium (Ti) to coordinate with phosphorus, forming stable metal–phosphorus complexes with remarkable air stability. Furthermore, studies have demonstrated that transition metals such as Cu, Fe, and Ti can coordinate with the lone pair electrons of phosphorus through the vacant orbitals of metal atoms, facilitating the formation of stable metal–phosphorus complexes.[31]

Metal–organic frameworks (MOFs) are crystalline hybrid materials composed of metal ions or clusters coordinated with organic ligands.[32–34] They feature well-defined periodic structures, ultrahigh-specific surface areas, and abundant nanoporous architectures.[35,36] The presence of transition metal ions in MOFs allows for coordination with the lone pair electrons on phosphorus atoms, effectively passivating BPNS surfaces and enhancing their environmental stability.[37] In addition, MOFs exhibit highly tunable structures. When MOFs with iron as the central metal node undergo pyrolysis in an inert atmosphere, they can spontaneously transform into magnetic carbon-based derivatives.[38] These MOF-derived carbonaceous materials inherit a low density, hierarchical porous architecture, excellent

tunability, strong magnetic properties, and superior dielectric loss capabilities, which are key features that contribute to enhanced magnetic loss mechanisms.[39] Furthermore, studies have shown that the introduction of cobalt (Co) promotes the valence state transition of metal species from higher to lower oxidation states, facilitating the formation of magnetic alloy nanoparticles with stronger magnetic responses.[40] This synergistic effect further enhances the microwave absorption performance of the resulting materials.

Inspired by the natural architecture of loofah sponges, we designed and fabricated a multifunctional carbon aerogel (CS-derived carbon/MOF@BPNS aerogel) that integrates microwave absorption, acoustic absorption, and infrared stealth functionalities. The loofah's structure consists of a lightweight, porous fibrous network that not only protects its seeds but also absorbs moisture while minimizing the overall weight of the fruit to reduce the burden on the plant. Analogously, in our material system, chitosan acts as the structural scaffold, akin to the loofah's fibrous flesh. It serves as both a protective matrix and a carrier for the MOF@BPNS composite, ensuring thermal insulation and sound absorption. Upon heating, chitosan can form a stable carbonaceous barrier, further enhancing the material's fire resistance. In this biomimetic model, black phosphorus nanosheets function as the functional seed, analogous to the loofah seed, providing the core electromagnetic absorption capability. Meanwhile, the FeCo-MOF serves as the protective shell for the BPNSs, forming uniform coatings on the BPNS surface through metal–phosphorus coordination interactions. This not only enhances the environmental stability of BPNSs but also introduces synergistic magnetic loss mechanisms, thereby improving the overall microwave absorption performance of the material. To prevent the aggregation of BPNS@MOF particles within the chitosan aerogel matrix, we drew inspiration from the loofah placenta, which is a structure that organizes seeds within the sponge. By introducing amino groups onto the MOF surface and employing glutaraldehyde as a cross-linker, we facilitated the formation of stable imine bonds (Schiff base linkages) between BPNS@MOF and the chitosan matrix. This strategy enabled the homogeneous dispersion of BPNS@MOF within the aerogel network. After mild carbonization, the resulting lightweight aerogel exhibited excellent multifunctional properties, including efficient microwave absorption, sound absorption, and infrared stealth capabilities.

2. Results and discussion

2.1. Synthesis and characterization

Scheme 1 illustrates the fabrication process of both the chitosan-derived carbon aerogel (CS-1) and the chitosan-derived carbon/BPNS@MOF aerogel (CS-2). Specifically, for the synthesis of CS-2, the FeCo-based metal–organic framework (FeCo-MOF) was first assembled onto the surface of black phosphorus nanosheets (BPNSs) *via* coordination between the exposed lone pair electrons on phosphorus atoms and the vacant orbitals of Fe and Co metal centers within the MOF structure. This strategy effectively forms BPNS@FeCo-MOF hybrids. Subsequently, the BPNS@FeCo-MOF hybrids were uniformly dispersed into a chitosan solution under vigorous stirring, followed by the addition of glutaraldehyde as a cross-linking agent. The resulting homogeneous mixture was cast into molds, rapidly frozen at −50 °C, and then subjected to

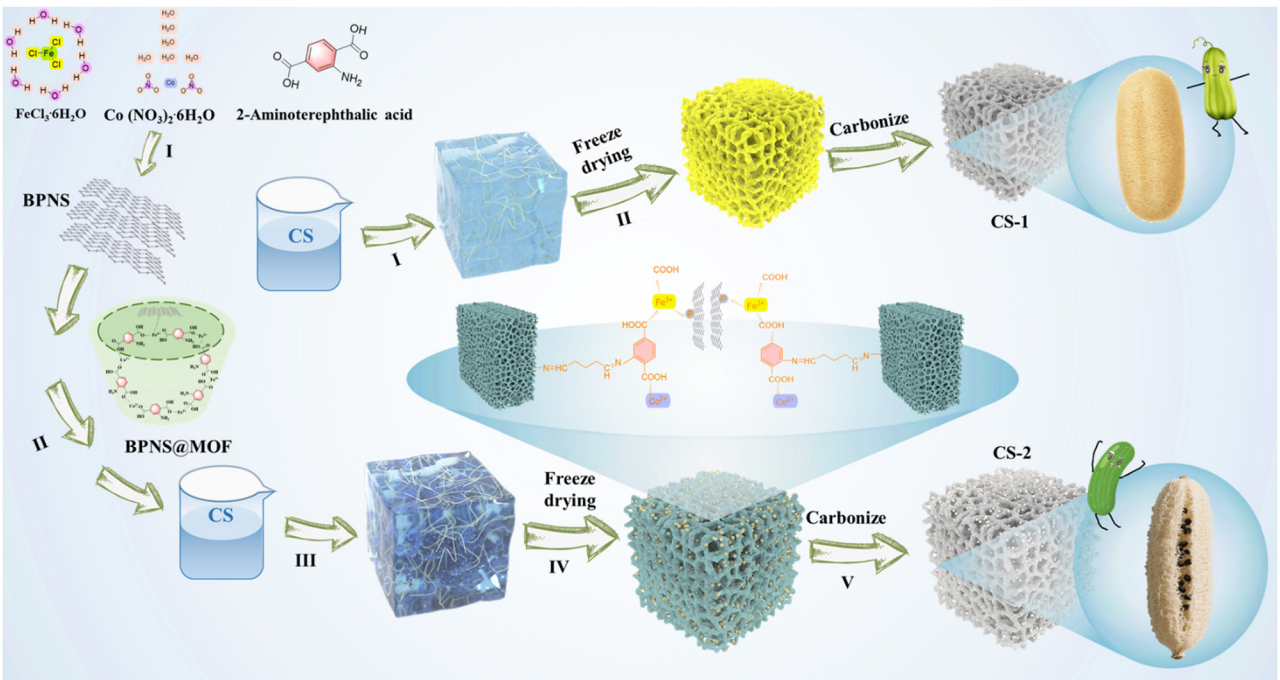

Scheme 1 Schematic illustration of the preparation process for the CS-derived carbon aerogel and CS-derived carbon/BPNS@MOF aerogel.

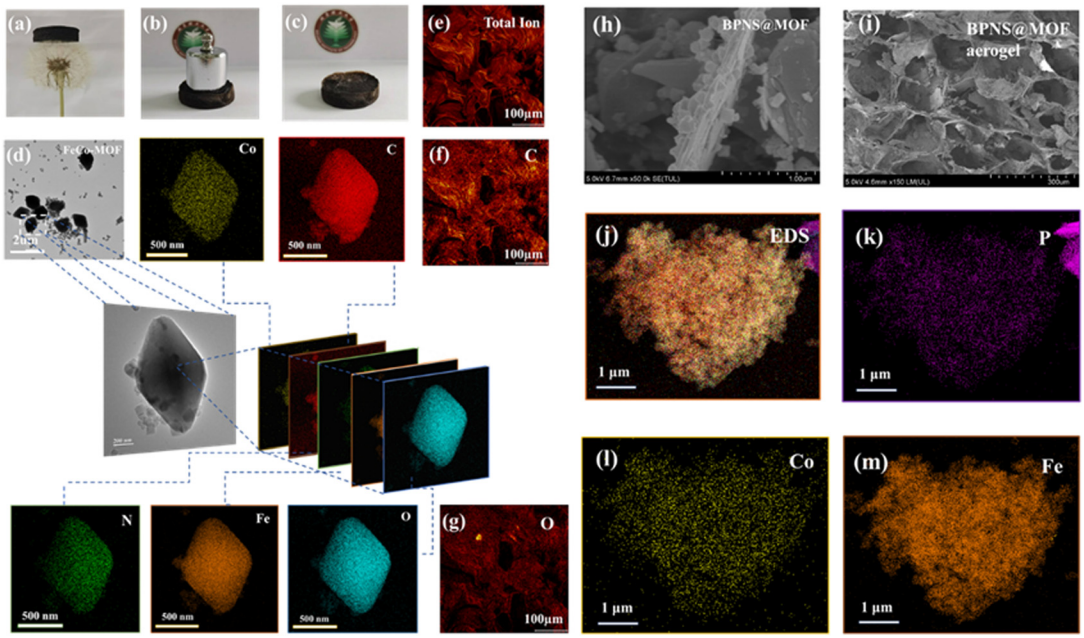

Fig. 1 (a) Digital photograph of CS-2; (b) and (c) mechanical performance demonstration of CS-2; (d) TEM image and EDS spectrum of FeCo-MOF; (e)–(g) TOF-SIMS mapping images of the CS-2 sample under UB mode (scale bar is 400 μm); (h) SEM image of BPNS@MOF; (i) SEM image of BPNS@MOF aerogel; (j)–(m) EDS mapping of BPNS@MOF.

freeze-drying to obtain the corresponding aerogel. The aldehyde groups in glutaraldehyde undergo nucleophilic addition reactions with the amino groups present on both chitosan and the MOF, forming imine bonds (Schiff bases) that create a robust three-dimensional network structure within the aerogel. This structural framework not only improves the dispersion of BPNS@MOF within the chitosan matrix but also enhances the mechanical strength, thermal stability, and water resistance of the aerogel. Finally, the as-prepared aerogel was carbonized at 800 °C under a nitrogen atmosphere, yielding the chitosan-derived carbon/BPNS@MOF aerogel (CS-2). As shown in Fig. 1(a), the obtained CS-2 aerogel exhibits a lightweight, cylindrical morphology. Remarkably, its mechanical robustness is demonstrated by its ability to be supported by a delicate dandelion seed without collapse while simultaneously bearing a 100 g weight without structural failure (Fig. 1(b) and (c)), underscoring its potential for practical applications in lightweight, multifunctional materials.

We first employed scanning electron microscopy (SEM) and transmission electron microscopy (TEM) to intuitively characterize the morphology and microstructure of the samples. As observed from high-resolution TEM and SEM images, FeCo-MOF exhibits a typical hexagonal rhombohedral structure, with Fe^{3+} and Co^{2+} species uniformly distributed within the nanocrystals, confirming the successful synthesis of FeCo-MOF (Fig. 1(d) and Fig. S1).[41] In the BPNS@MOF nanosheets, BPNSs serve as a template at the bottom, while FeCo-MOF nanoparticles are uniformly anchored on the BPNS surface (Fig. 1(h)). This structural configuration is further verified by energy-dispersive X-ray spectroscopy (EDS) elemental mapping, as shown in Fig. 1(j)–(m) and Fig. S2, the elements C, O, N, Co, Fe, and P exhibit homogeneous distributions, which is consistent with our design hypothesis. Subsequently, SEM was used to examine the freeze-dried pure chitosan aerogel and the chitosan aerogel incorporated with BPNS@MOF. Compared with the pure chitosan aerogel, the BPNS@MOF-modified aerogel displays a more regular three-dimensional porous network structure, with BPNS@MOF uniformly coating the aerogel framework, which can be attributed to the introduction of amino groups on the MOF surface (Fig. 1(i) and Fig. S3a–c). Finally, after carbonization, the aerogels maintain a well-defined three-dimensional porous network structure, as shown in Fig. S3d and e. Notably, the CS-2 aerogel exhibits a more ordered and denser pore distribution, further corroborating the aforementioned observations.

Subsequently, to further elucidate the microstructure and elemental distribution of the CS-2 aerogel, we employed time-of-flight secondary ion mass spectrometry (TOF-SIMS) for detailed surface characterization. The two-dimensional ion imaging results are presented in Fig. 1(e)–(g) and Fig. S4. The color bar on the right indicates the relative intensity of the ion signals, with colors transitioning from black to red corresponding to increasing signal intensity; ''Max'' and ''0'' represent the maximum and minimum ion intensities, respectively. The TOF-SIMS secondary ion images reveal that the carbonized CS-2 sample exhibits a honeycomb-like wrinkled morphology with irregularly distributed pores over a 400 μm scale, corroborating the SEM observations. Furthermore, in combination with SEM images, we observed that the pore sizes range from several millimeters or tens of micrometers down to hundreds of nanometers. This multiscale pore size distribution is advantageous for enhancing electromagnetic wave attenuation by

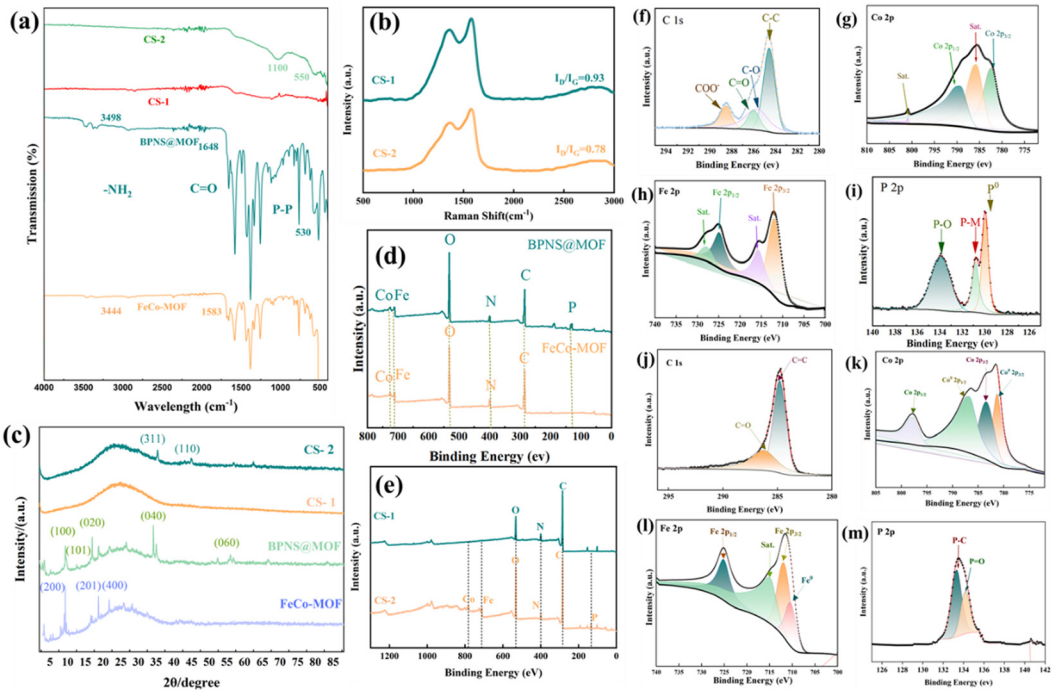

Fig. 2 (a) FTIR spectra of FeCo-MOF, BPNS@MOF, CS-1, and CS-2; (b) Raman spectra of CS-1 and CS-2; (c) XRD patterns of FeCo-MOF, BPNS@MOF, CS-1, and CS-2; (d) XPS survey spectra of FeCo-MOF and BPNS@MOF; (e) XPS survey spectra of CS-1 and CS-2; (f)–(i) high-resolution XPS spectra of individual elements in BPNS@MOF; (j)–(m) high-resolution XPS spectra of individual elements in CS-2.

providing multiple scattering centers and facilitating energy dissipation. The elemental distribution maps further reveal that the CS-2 aerogel predominantly comprises carbon and oxygen, outlining the basic morphology of the sample and confirming the successful carbonization process. Notably, the key elements Fe, Co, and P are also homogeneously distributed throughout the aerogel, which aligns well with our previous assumption regarding the uniform dispersion of fillers within the material.

To further elucidate the structural characteristics of the materials, Fourier transform infrared spectroscopy (FTIR), X-ray diffraction (XRD), and X-ray photoelectron spectroscopy (XPS) analyses were conducted. The FTIR spectrum of FeCo-MOF, as shown in Fig. 2(a), exhibits characteristic peaks at 1648 cm^{-1} and 1200 cm^{-1}, which are attributed to the stretching vibrations of C═O and C–O bonds, respectively. Additionally, peaks at 1450 cm^{-1} and 769 cm^{-1} arise from the vibrational modes of the benzene ring, indicating the successful coordination of 2-amino terephthalic acid and thereby confirming the formation of FeCo-MOF.[20,30] The broad absorption band observed around 3400 cm^{-1} corresponds to the N–H stretching vibration, further verifying the incorporation of amino groups into the framework.[42] Compared with FeCo-MOF, the FTIR spectrum of BPNS@MOF shows a weak characteristic peak at approximately 500 cm^{-1}, which can be attributed to the P–P vibrational mode, suggesting the successful integration of BPNSs into the MOF structure. In the case of the CS-2 aerogel, distinct absorption bands appear at around 1100 cm^{-1} and 600 cm^{-1}, corresponding to the characteristic vibrations of P–O, P–P, and M–O (M represents Fe or Co) bonds. These findings provide indirect evidence for the successful incorporation of BPNS@MOF nanosheets into the aerogel matrix and the formation of magnetic nanoparticles.[43] The Raman spectra of CS-1 and CS-2 aerogels are shown in Fig. 2(b), where the two prominent peaks at approximately 1300 cm^{-1} and 1600 cm^{-1} correspond to the D and G bands, respectively. The intensity ratio of these peaks (I_D/I_G) is commonly used as an indicator of the degree of carbonization, where a lower I_D/I_G value implies higher graphitization, fewer defects, and better carbon network ordering.[44] Notably, the CS-2 sample exhibits a lower I_D/I_G ratio compared to CS-1, indicating a higher degree of carbonization. This enhancement is primarily attributed to the catalytic graphitization effect of the FeCo-MOF component during the carbonization process.

The XRD results, which complement the FTIR findings, provide further evidence of the successful synthesis of the materials. As shown in Fig. 2(c), the characteristic diffraction peaks at $2\theta \approx 9.1^\circ$ and 11.4°, corresponding to the (100) and (101) planes, are consistent with previously reported patterns for FeCo-MOF, confirming its successful formation.[45] In the XRD pattern of BPNS@MOF, distinct peaks appear at 16.7°, 37.4°, and 52.4°, which can be assigned to the (020), (040), and (060) planes of black phosphorus, respectively. This result validates the successful incorporation of BPNSs into the composite structure.[46] Furthermore, the XRD patterns of the CS-1 and CS-2 aerogels exhibit a broad diffraction peak centered around 52.4°, which is characteristic of amorphous carbon, indicating the successful carbonization of the aerogels. In the case of the CS-2 aerogel, additional diffraction peaks corresponding to the (110) and (200) planes of FeCo alloy, as well as

the (311), (440), and (511) planes of magnetite (Fe_3O_4), are clearly observed. These features confirm the formation of magnetic nanoparticles within the aerogel matrix, which is consistent with the results obtained from FTIR analysis and further supports the successful integration of FeCo-based components into the carbonized aerogel network.[47]

To further elucidate the chemical states and bonding configurations of the elements in the synthesized materials, X-ray photoelectron spectroscopy (XPS) and high-resolution spectra were conducted. As shown in Fig. 2(d), the presence of phosphorus in the BPNS@MOF composite confirms the successful incorporation of BPNSs. The detailed analysis of the C 1s (Fig. 2(f)), Co 2p (Fig. 2(g)), Fe 2p (Fig. 2(h)), and P 2p (Fig. 2(i)) spectra provides further evidence supporting the structural integrity of the BPNS@MOF. Specifically, the C 1s spectrum exhibits a characteristic peak at 288.5 eV, corresponding to the C═O bond from the carboxylate group, indicative of successful ligand coordination. The Co 2p spectrum displays peaks at 782.1, 785.6, 789.7, and 801.8 eV, which can be attributed to the Co $2p^{3/2}$ and Co $2p^{1/2}$ spin–orbit components of divalent Co^{2+}. Similarly, the Fe 2p spectrum shows peaks at 711.8, 716.0, 725.1, and 728.2 eV, corresponding to the Fe $2p^{3/2}$ and Fe $2p^{1/2}$ signals of trivalent Fe^{3+}.[48] These results collectively confirm the successful coordination between metal ions and oxygen atoms, indicating the successful synthesis of FeCo-MOF. In addition, the P 2p spectrum exhibits a peak at 131 eV, confirming the coordination of phosphorus with metal species, which is consistent with our proposed design, while the peak at 134 eV corresponds to the P–O bond, which may arise from partial oxidation of phosphorus during synthesis. The N 1s spectrum shows a peak at 399.2 eV, further confirming the successful incorporation of amino groups, in agreement with the FTIR results (Fig. S5).[49] For the CS-2 aerogel (Fig. 2(e)), the detection of Fe, Co, and P signals further supports the successful incorporation of BPNS@MOF nanosheets into the carbon aerogel matrix. The observed changes in the C 1s peak intensity also confirm the successful carbonization of the aerogel, corroborating the findings from Raman and XRD analyses. The high-resolution spectra of Fe and Co provide further evidence for the formation of magnetic nanoparticles. Specifically, the Co 2p spectrum exhibits distinct peaks at 778.9 eV and 798.9 eV, which can be attributed to metallic cobalt (Co^0), while the Fe 2p spectrum shows a characteristic peak at 707.9 eV, corresponding to metallic iron (Fe^0). These findings unequivocally confirm the successful formation of FeCo magnetic nanoparticles within the carbon aerogel matrix, as illustrated in Fig. 2(j)–(m).

In addition, we conducted a comprehensive investigation into the thermal properties, pore size distribution, and porosity of the synthesized functional fillers and composite aerogels. To determine the pore structure and porosity, nitrogen adsorption–desorption isotherms were recorded for FeCo-MOF and BPNS@MOF. As shown in Fig. 3(a) and (b), both materials exhibit characteristic adsorption–desorption curves and corresponding pore size distribution profiles. The results indicate that the synthesized fillers retained a well-defined nanoporous structure. Specifically, FeCo-MOF displayed a high specific surface area exceeding 766 $m^2\ g^{-1}$, with an average pore size of approximately 2.7 nm. Upon assembly with BPNS, although the surface area slightly decreased to 372 $m^2\ g^{-1}$, the average pore size remained around 2.4 nm. After incorporation into the chitosan aerogel matrix followed by carbonization, the resulting aerogels exhibited a more compact pore structure due to the carbon-rich framework. The final aerogel possessed a high porosity of up to 96% with a low bulk density of 0.026 g cm^{-3}, providing a robust structural basis for the enhancement of multifunctional properties. Subsequent thermogravimetric (TG) analysis demonstrated that both FeCo-MOF and BPNS@MOF fillers exhibited excellent

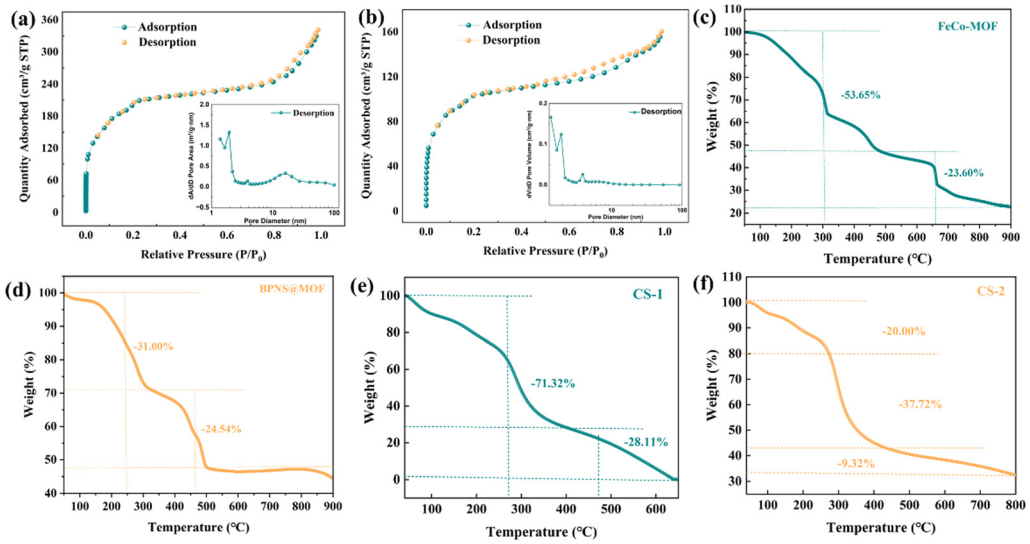

Fig. 3 (a) Nitrogen adsorption–desorption isotherm (BET curve) of FeCo-MOF; (b) nitrogen adsorption–desorption isotherm (BET curve) of BPNS@MOF; (c) thermogravimetric (TG) curve of FeCo-MOF; (d) thermogravimetric (TG) curve of BPNS@MOF; (e) thermogravimetric (TG) curve of CS-1; (f) thermogravimetric (TG) curve of CS-2.

thermal stability, with characteristic two-step decomposition behavior (Fig. 3(c) and (d)). Notably, the BPNS@MOF composite exhibited improved thermal resistance compared to pristine BPNS, retaining nearly 50% of its original weight after the second decomposition stage. When incorporated into the aerogel framework, the composite aerogel showed a significant increase in decomposition temperature relative to the pure chitosan aerogel, confirming the enhancement in thermal stability imparted by the hybrid filler system (Fig. 3(e) and (f)).

2.2. Microwave absorption performance

The effective absorption bandwidth (EAB) and reflection loss (RL) intensity are two critical metrics for evaluating the overall microwave absorption performance of microwave-absorbing materials (MAMs).[50] The EAB represents the continuous frequency range over which the RL value remains below a specified threshold at a given thickness, while the RL intensity quantifies the attenuation of incident electromagnetic waves by the material. The RL value is calculated according to eqn (1):

$$\mathrm{RL}\ (\mathrm{dB}) = 20 \log \left| \frac{Z_{\mathrm{in}} - Z_0}{Z_{\mathrm{in}} + Z_0} \right| \quad (1)$$

For practical applications, RL values lower than −10 dB are considered effective.[51] To further elucidate the microwave absorption mechanism of our hybrid nanofillers, we also prepared a carbonized aerogel incorporating BPNSs under the same conditions, denoted as CS_{BP}. The three-dimensional RL plots of the samples are presented in Fig. 4(a)–(c). In these plots, the extent and continuity of the dark blue regions indicate the breadth and effectiveness of microwave absorption. All aerogel samples possess a certain degree of electromagnetic energy dissipation capability, though their performance varies significantly. For instance, CS-1 exhibits sparse and discontinuous dark blue regions and only achieves a minimum RL (RL_{min}) of

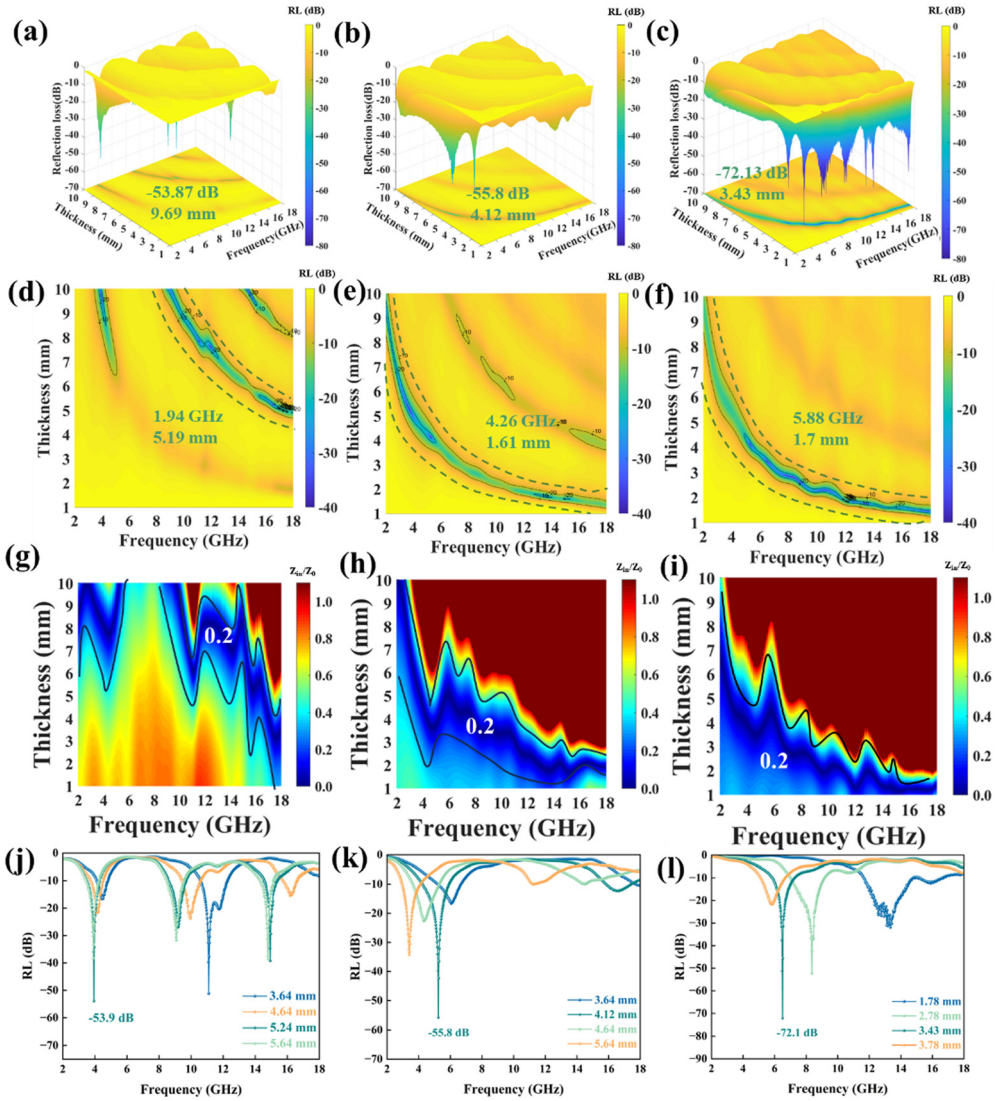

Fig. 4 3D and 2D reflection loss (RL) curves of (a and d) CS-1, (b and e) CS_{BP} and (c and f) CS-2; impedance matching ($|\Delta|$) of (g) CS-1, (h) CS_{BP} and (i) CS-2; RL values of the effective absorption bandwidth (EAB) at selected absorber thicknesses for (j) CS-1, (k) CS_{BP} and (l) CS-2.

−53.87 dB at 3.94 GHz when the absorber thickness reaches 9.69 mm. In contrast, CS_{BP} shows an improved absorption performance, with an RL_{min} of −55.8 dB at 5.24 GHz under a reduced thickness of 4.12 mm. This improvement is visually manifested in the form of increased and more continuous dark blue regions in the RL maps. Notably, CS-2 demonstrates the most outstanding performance, achieving an RL_{min} as low as −72.13 dB at 6.5 GHz with a significantly thinner absorber thickness of just 3.43 mm. Furthermore, CS-2 also exhibits superior EAB performance. As shown in the two-dimensional RL contour maps (Fig. 4(d)–(f)), CS-2 achieves a broader and more continuous absorption bandwidth compared to CS-1 (1.94 GHz at 16.06–18 GHz, 5.19 mm) and CS_{BP} (4.26 GHz at 13.02–17.28 GHz, 1.61 mm). Specifically, CS-2 reaches an impressive EAB of 5.88 GHz (12–17.88 GHz) at a thickness of merely 1.7 mm, highlighting its potential as an effective broadband microwave absorber. Additionally, Fig. 4(j)–(l) further demonstrates that CS-2 maintains excellent absorption performance across a wider range of thicknesses. Comparative analysis with recently reported materials further underscores the outstanding electromagnetic wave (EMW) absorption properties of CS-2 (Fig. S6). Compared to other aerogel-based EMW absorbing materials, CS-2 exhibits the lowest RL_{min} values, outperforming the majority of reported EMW absorbers and showcasing its remarkable promise for practical applications in this field.

Efficient impedance matching is a fundamental prerequisite for the effective entry of incident microwaves into an absorber, while a high attenuation constant ensures the material's ability to dissipate the absorbed electromagnetic energy. These two factors work synergistically and complement each other to determine the overall microwave absorption performance.[52] To further elucidate the microwave absorption mechanism of the materials, we systematically analyze these two aspects. As previously discussed, excellent impedance matching is a critical parameter in evaluating a material's absorption capability. For optimal microwave entry into the absorber, the characteristic impedance of the material Z_{in} must match that of free space Z_0. This relationship can be quantified by the following equation:

$$|\Delta| = |\sinh^2(Kfd) - M| \tag{2}$$

$$K = \frac{4\pi\sqrt{\mu_r\varepsilon_r}\sin\dfrac{\delta_e+\delta_m}{2}}{c\cdot\cos\delta_e\cos\delta_m} \tag{3}$$

$$M = \frac{4\mu_r'\cos\delta_e\varepsilon_r'\cos\delta_m}{\left(\mu_r'\cos\delta_e-\varepsilon_r'\cos\delta_m\right)^2+\left[\tan\left(\dfrac{\delta_m}{2}-\dfrac{\delta_e}{2}\right)\right]^2\left(\mu_r'\cos\delta_e+\varepsilon_r'\cos\delta_m\right)^2} \tag{4}$$

when the value of $|\Delta|$ approaches zero, the impedance matching is considered ideal; typically, $|\Delta| < 0.2$ is regarded as sufficient for effective microwave absorption.[53] As shown in Fig. 4(g)–(i), the $|\Delta|$ values of the samples exhibit distinct differences. Notably, CS_{BP} and CS-2 display extensive and continuous dark blue regions at relatively thin absorber thicknesses, with CS-2 demonstrating the most optimal impedance-matching behavior. This indicates that, at reduced thicknesses, the incident microwaves can effectively penetrate the absorbing material, confirming the excellent impedance-matching capability of these systems. In contrast, the CS-1 sample exhibits narrow and discontinuous blue regions, which only emerge at higher thicknesses. This suggests that a significant portion of the incident electromagnetic waves are reflected at the material's surface, resulting in a substantial decrease in absorption efficiency. The enhanced impedance matching in CS_{BP} and CS-2 can be attributed to the synergistic contributions of BPNSs and their derivatives. Additionally, the incorporation of magnetic nanoparticles further optimizes the electromagnetic parameter ratio, thereby achieving superior impedance matching capabilities. The layered structure and moderate conductivity of BPNSs enable fine-tuning of the dielectric properties and enhancement of interfacial polarization, while the incorporation of magnetic nanoparticles further optimizes the electromagnetic parameter ratios, collectively leading to superior impedance matching characteristics.

Once microwaves penetrate into the material, it is essential that the material possesses sufficient capability to attenuate and dissipate the electromagnetic energy. This intrinsic attenuation capability is quantitatively evaluated by the attenuation constant (α), as shown in Fig. S7 and S8.[54] All samples exhibit an increasing trend in α with rising frequency, indicating enhanced microwave attenuation performance at higher frequencies. Notably, the α values of CS-2 are significantly higher than those of CS-1 and CS_{BP} across the entire measurement frequency range, demonstrating the superior inherent attenuation capability of CS-2, which is consistent with the RL performance discussed previously. Electromagnetic parameters play a crucial role in elucidating the inherent attenuation mechanisms of the absorber.[55] Fig. 5(a) and (b) illustrates the frequency-dependent trends of the real part (ε') and imaginary part (ε'') of the dielectric constant, where ε' represents the capacity for energy storage, and ε'' reflects the capacity for energy dissipation. It can be observed that both ε' and ε'' of CS_{BP} and CS-2 decrease gradually with increasing frequency, a trend that aligns with the typical behavior of dielectric-dominated microwave absorbing materials. In contrast, the ε' and ε'' values of CS-1 exhibit minimal variation or even a slight increase with increasing frequency. This behavior is primarily due to the material's structure being dominated by a carbon skeleton, resulting in a relatively simple architecture with limited polarization mechanisms, which are mainly restricted to conductive polarization and a minor contribution from interfacial polarization. Moreover, the ε' and ε'' values of CS-2 and CS_{BP} are considerably higher than those of CS-1, indicating their superior capacities for dielectric energy storage and loss. This enhancement is ascribed to the dipolar and interfacial polarization effects introduced by the incorporation of BPNSs and their derivatives. Additionally, the ε' and ε'' curves of CS-2 display pronounced fluctuation peaks in the 6.0–18.0 GHz range. Typically, the fluctuations observed between 6.0 and 10.0 GHz arise from dipolar relaxation processes, while those in the 10.0–18.0 GHz range are primarily due to interfacial polarization relaxation.[56] These observations suggest that

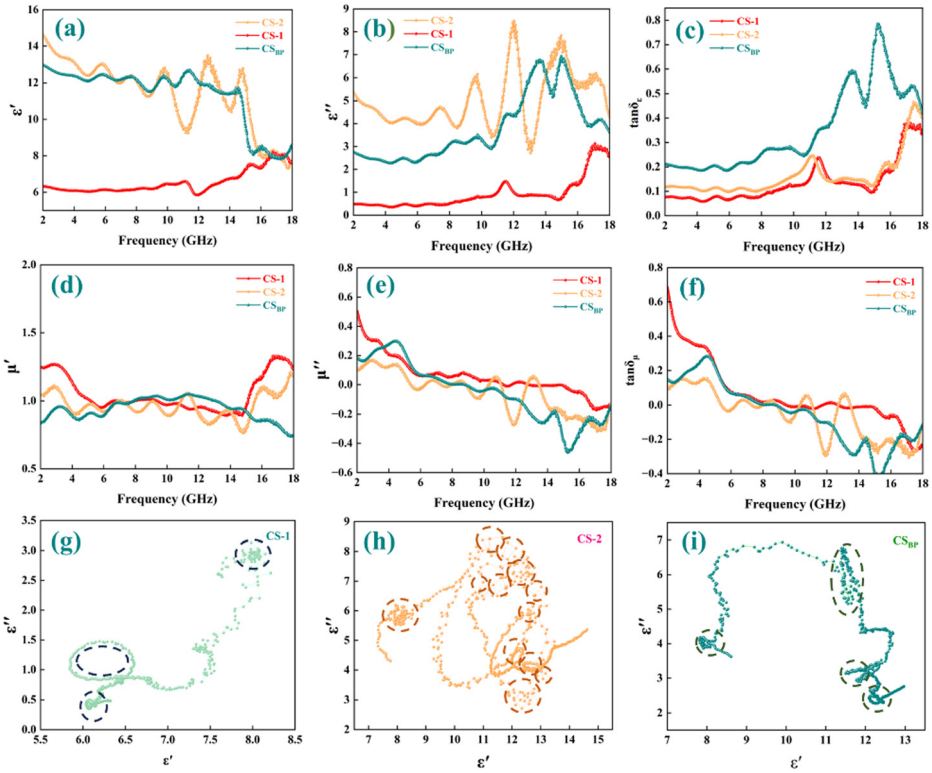

Fig. 5 (a) and (b) Real and imaginary parts of the complex permittivity; (c) dielectric loss tangent; (d) and (e) real and imaginary parts of the complex permeability; (f) magnetic loss tangent; (g) Cole–Cole plots of CS-1; (h) Cole–Cole plots of CS-2; (i) Cole–Cole plots of CS_{BP}.

the asymmetric coordination structures within the MOF and its derivatives enhance the dipolar response capability of the material. Simultaneously, the increased interfacial area promotes stronger interfacial polarization relaxation effects.

The relaxation processes of the samples are further analyzed using the Debye theory, as illustrated by the Cole–Cole plots in Fig. 5(g)–(i). Each semicircular arc corresponds to a distinct relaxation process, while the linear tail at the end of the curves indicates conductive loss contributions. Evidently, the Cole–Cole plots of CS-2 display a greater number and more pronounced semicircles compared to other samples, indicating the presence of multiple relaxation processes. This observation corroborates the numerous fluctuation peaks observed in the ε' and ε'' curves (Fig. 5(a) and (b)). Furthermore, the appearance of linear tails in the CS-2 and CS_{BP} samples suggests that electrons can migrate and hop within the three-dimensional conductive networks, contributing to significant conductive loss behavior. Therefore, the exceptional dielectric loss properties of the CS-2 aerogel can be ascribed to the synergistic effects of strong polarization loss and conductive loss.

To more accurately evaluate the relative contributions of different dielectric loss mechanisms, the polarization loss (ε_p'') and conduction loss (ε_c'') were calculated based on Debye theory using eqn (S9) and (S10).[57–59] As shown in Fig. S11, CS-2 exhibits a moderate level of conduction loss compared to CS-1, which can be attributed to the enhanced electronic conductivity introduced by BPNS. Moreover, the presence of multiple heterogeneous interfaces in the CS-2 system (particularly between the aerogel matrix and BPNS, as well as between BPNS and MOF) leads to pronounced interfacial polarization. Under an alternating electromagnetic field, charge accumulation at these interfaces intensifies the polarization effect, resulting in a polarization loss ratio exceeding 89% of the total dielectric loss, indicating that polarization loss is the dominant mechanism in these samples. Notably, the value of ε_p'' increases with frequency, which helps suppress the dispersion effect.[60] As a result, the overall ε'' remains at a moderate level across the 2–18 GHz frequency range, thereby endowing the CS-2 sample with excellent broadband microwave absorption performance. Fig. 5(c) depicts the frequency-dependent variation of the dielectric loss tangent ($\tan\delta_\varepsilon = \varepsilon''/\varepsilon'$). The $\tan\delta_\varepsilon$ value of CS-2 surpasses that of CS-1, further confirming its stronger dielectric attenuation capability. However, it remains lower than that of CS_{BP}, likely due to the abundance of in-plane and edge defects as well as vacancies present in BPNSs and their derivatives, which significantly enhance the dielectric loss of CS_{BP}.[61]

In addition to dielectric loss, magnetic loss is another key factor influencing the attenuation capability. Fig. 5(d)–(f) presents the frequency-dependent real (μ') and imaginary (μ'') parts of the complex permeability and the magnetic loss tangent ($\tan\delta_\mu = \mu''/\mu'$) for all samples. It can be observed that all samples exhibit similar μ', μ'', and $\tan\delta_\mu$ values. Notably, the CS-2 sample displays pronounced fluctuation peaks in the 6.0–14.0 GHz frequency range, indicating significant magnetic resonance phenomena within the composite system. This behavior is likely attributed to the highly dispersed FeCo

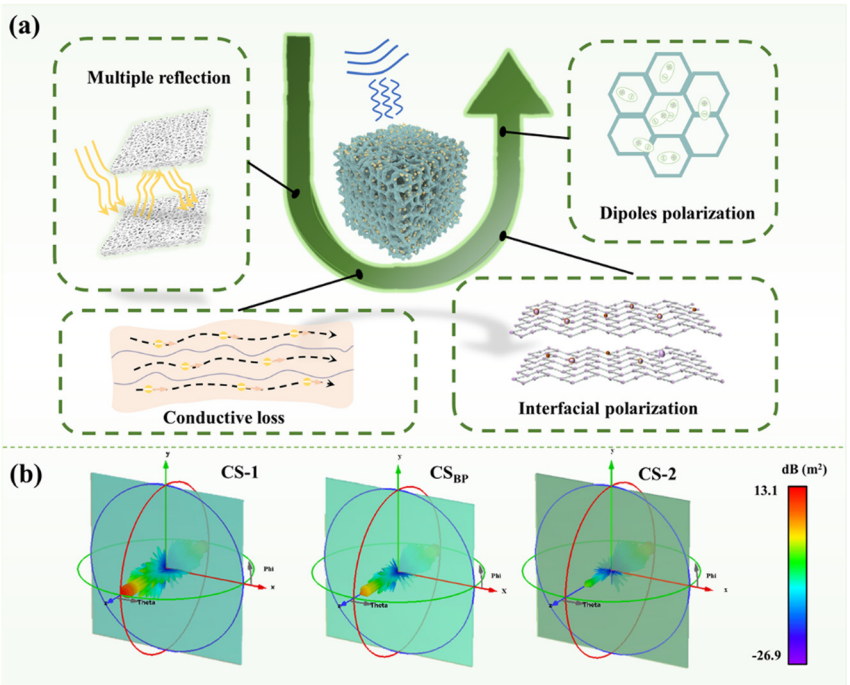

Fig. 6 (a) Schematic illustration of the electromagnetic wave absorption mechanism of the CS-2 aerogel; (b) RCS simulation images of CS-1, CS$_{BP}$, CS-2.

nanoparticles on the MOF-derived substrates and the synergistic interfacial structure formed with BPNSs, which effectively enhances the magnetic loss mechanism.[62] This also explains why the tan δ_ε value of CS-2 is slightly lower than that of CS$_{BP}$, while still achieving superior overall absorption performance. Furthermore, the tan δ_ε value of CS-2 is evidently higher than its tan δ_μ, demonstrating that dielectric loss predominantly contributes to its excellent microwave attenuation properties. Overall, the mechanism can be attributed to several synergistic factors (Fig. 6(a)). Firstly, the aerogel's highly porous and interconnected channel structure facilitates excellent impedance matching, thereby allowing more incident electromagnetic waves to penetrate into the absorber. As the waves propagate further, they undergo multiple internal reflections and scattering within the porous channels, effectively enhancing wave attenuation. In addition, the migration of charge carriers within the conductive black phosphorus layer contributes significantly to conduction loss. Finally, the abundant heterogeneous interfaces induce interfacial polarization, which markedly enhances polarization loss.[63]

Finally, to further validate the practical application potential of the CS-2 aerogel, we conducted electromagnetic simulations using CST software. A flat plate model with dimensions of 40 mm × 40 mm was constructed, and the thickness was set according to the previously determined optimal reflection loss conditions. The electromagnetic parameters of each aerogel sample were then incorporated into the simulation model, and the resulting outcomes are presented in Fig. 6(b). S12 illustrates the simulated radar cross-section (RCS) profiles of perfect electric conductor (PEC) plates coated with CS-1, CS$_{BP}$, and CS-2 aerogels, respectively. The horizontal axis denotes the angle of incidence, and the frequency was set at 9.44 GHz. The simulation results reveal varying degrees of scattering signals across the samples. Specifically, the CS-1 sample exhibits the strongest scattering response, whereas the CS-2 sample demonstrates the lowest RCS values. For the CS-2-coated plate, the RCS remains below −10 dB m^2 across a broad angular range of −125° to −25° and 25° to 125°, while the CS-1-coated plate only achieves RCS values below −10 dB m^2 within narrower angular windows of −100° to −50° and 50° to 100°. These findings are consistent with the earlier experimental results, further confirming the superior microwave absorption performance of the CS-2 sample. Fig. S13 presents a histogram of the RCS values at selected incidence angles for each sample, offering a more intuitive comparison. The results clearly illustrate that CS-2 maintains lower RCS values over a broader range of incidence angles, underscoring its exceptional potential for practical applications in microwave absorption and stealth technologies.

2.3. Thermal insulation performance

For electromagnetic wave (EMW) absorbing materials to be effectively employed in complex and variable environments, they must exhibit additional functionalities beyond absorption performance, such as thermal insulation and infrared stealth capabilities.[64] Among these, thermal conductivity (λ) is a critical parameter, as it quantifies a material's ability to conduct heat under a unit temperature gradient and serves as a key indicator of its thermal insulation performance.[65] To evaluate this property, we measured the thermal conductivities of the CS-1 and CS-2 aerogels. As shown in Fig. 7(a), both samples exhibited remarkably low thermal conductivities, with the CS-2

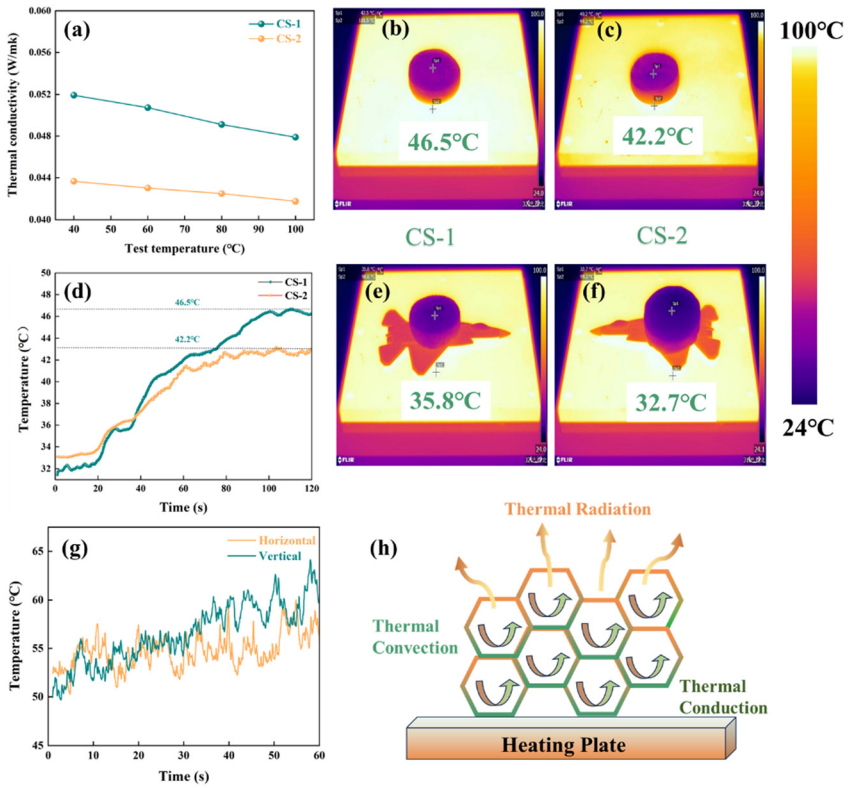

Fig. 7 (a) Thermal conductivity curves of CS-1 and CS-2; (b and c) infrared thermal images (IR) of CS-1 and CS-2 aerogel samples after 2 min on a 100 °C heating plate; (d) temperature profiles of CS-1 and CS-2 at different time points on a 100 °C heating plate; (e) and (f) infrared thermal images (IR) of CS-1 and CS-2 aerogel samples after 2 min on a 100 °C heating plate; (g) temperature profiles along the radial and axial directions at different time points on a 100 °C heating plate; (h) schematic of the thermal transfer mechanism of the CS-2 composite aerogel in the radial and axial directions.

aerogel demonstrating an even lower value than CS-1, achieving a thermal conductivity of less than 0.05 W (m K)$^{-1}$. This superior thermal insulation can be understood by considering the fundamental heat transfer mechanisms in porous materials, where the overall thermal conductivity is the sum of four contributions: solid-phase conduction (λ_s), gas-phase conduction (λ_g), radiative conduction (λ_r), and convective conduction (λ_c), expressed as follows:

$$\lambda = \lambda_s + \lambda_g + \lambda_c + \lambda_r \quad (5)$$

For porous materials with pore sizes smaller than 1 mm, the convective term (λ_c) is typically negligible and can thus be excluded from the total thermal conductivity expression.[66] Consequently, the equation simplifies to

$$\lambda = \lambda_s + \lambda_g + \lambda_r \quad (6)$$

The extremely low thermal conductivity of the aerogels in this study can be primarily attributed to their highly porous structures, which hinder gas flow and extend the heat transfer pathways, thereby effectively reducing λ_g. Additionally, in aerogels, phonon transport dominates solid-phase thermal conduction (λ_s). The presence of abundant nanoscale grains formed by the carbonization of BPNS@MOF within the CS-2 aerogel introduces a high density of grain boundaries that act as scattering centers for phonons. This phonon scattering significantly limits the phonon mean free path, thereby suppressing thermal conduction and further lowering λ_s. The combination of nanoscale grain-induced phonon scattering and the aerogel's intrinsic porous architecture synergistically contributes to the remarkably low thermal conductivity observed in the CS-2 aerogel.

To evaluate the infrared stealth capabilities of the composite aerogels, we placed the samples on a heating plate maintained at 100 °C and recorded both their temperature evolution curves and infrared thermal images, as shown in Fig. 7(b)–(d). From the time–temperature profiles, it is evident that, compared to CS-1, the CS-2 aerogel exhibits a broader and more stable plateau in radiation temperature, with a lower surface temperature that stabilizes around 40 °C. This performance can be attributed to the nanoscale fibrous network within the CS-2 aerogel, as well as the interfaces between the nanofibers and embedded nanoparticles. These interfaces act as phonon scattering centers, enhancing interfacial thermal resistance and further reducing solid-phase thermal conductivity, thus endowing CS-2 with exceptional potential for infrared stealth applications.[67] To further demonstrate the practical infrared stealth capability of the CS-2 aerogel, we applied a 20.0 ± 0.2 mm thick CS-2 onto a model aircraft and assessed its thermal camouflage performance, as depicted in Fig. 7(e) and (f). The corresponding infrared thermal images reveal that the CS-2 effectively reduces the radiation temperature from 40 °C to

32 °C, rendering it nearly indistinguishable from the ambient temperature and maintaining this effect over an extended period. This confirms the material's capability for sustained thermal camouflage.

Furthermore, Fig. 7(g) and Fig. S14 present the time–temperature profiles and corresponding infrared thermal images of CS-3 (oriented perpendicular to the ice crystal growth direction) and CS-4 (oriented parallel to the ice crystal growth direction) aerogels, each with a thickness of 2.0 ± 0.2 mm, placed on a 100 °C heating plate. Interestingly, the anisotropic microstructures result in distinct thermal insulation behaviors between the two samples. Specifically, at the same heating duration, the surface temperature of CS-3 is higher than that of CS-4. This can be attributed to the alignment of the oriented channel structure with the heat transfer direction in CS-4, facilitating more efficient heat conduction along the cell walls. Conversely, when the heat transfer direction is perpendicular to the alignment of tubular channels (as in CS-3), the presence of numerous directional pores impedes heat flow, thereby reducing thermal conductivity, as illustrated in Fig. 7(h).[68–70]

2.4. Sound absorption performance

In contemporary society, noise has emerged as a significant pollutant that adversely affects human quality of life. In engineering and industrial sectors, such as automotive, rail transit, and aerospace, noise control has become a critical criterion for evaluating product performance and user experience.[71] However, the simultaneous achievement of excellent thermal insulation and acoustic absorption remains a formidable challenge. Beyond demonstrating the superior thermal insulation performance of our CS aerogels, we also verified their remarkable acoustic absorption capabilities. To evaluate this property under realistic conditions, we constructed a simulation model mimicking everyday scenarios, including aircraft takeoff, landing, and in-flight cabin noise. This experimental setup involved connecting a smartphone to a Bluetooth speaker, placing the speaker within a custom-fabricated aerogel enclosure installed in an aircraft model, and playing various soundtracks corresponding to different noise environments. For the simulation of in-cabin noise, we selected scenarios such as noise during aircraft takeoff, landing, objects dropping, and striking a tabletop. As shown in Fig. 8(a), all measured decibel values were significantly reduced, approaching the baseline levels of ambient noise within the laboratory. This outcome underscores the excellent acoustic-damping performance of the CS aerogels under realistic noise conditions.

To further validate the superior sound absorption performance of the modified chitosan aerogels, a transfer function sound absorption coefficient testing system was employed for

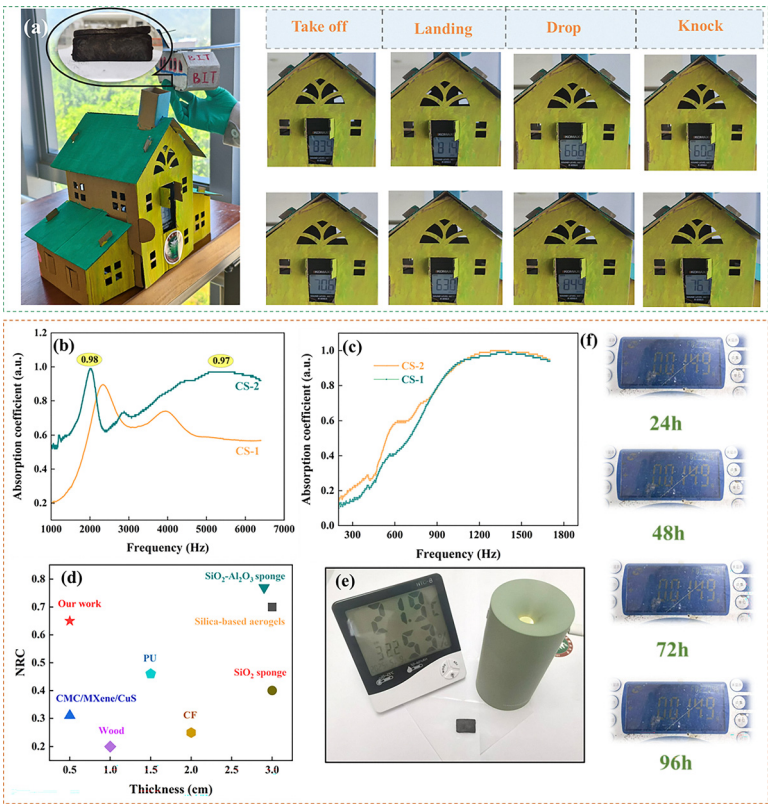

Fig. 8 (a) Noise reduction test of the CS-2 aerogel under different scenarios: airplane take off, airplane landing, heavy object dropping, and table knocking; (b) sound absorption coefficient curves in the high-frequency range; (c) sound absorption coefficient curves in the low-frequency range; (d) comparison of the NRC between CS-2 and related absorbers; (e) experimental setup for high-humidity testing; (f) results of the high-humidity testing experiment.

high-frequency measurements (Fig. 8(b)).[72] The results indicate that the modified aerogels exhibit remarkable sound absorption capabilities, particularly within the 2000 Hz and 4500–6500 Hz frequency bands, where a 5.0 mm thick sample achieved a sound absorption coefficient exceeding 0.95. This performance significantly surpasses that of the pristine aerogel, highlighting the enhanced acoustic properties imparted by the modification. As shown in Fig. 8(c), the sound absorption coefficients of the samples at lower frequencies reveal that the CS-2 aerogel also slightly outperforms CS-1 in the low-frequency regime. Moreover, the noise reduction coefficient (NRC), which is a measure of the average sound absorption coefficients at 250, 500, 1000, and 2000 Hz, can also be used to assess the acoustic performance of porous materials.[73] As expected, the results further confirm the superior sound absorption performance of the modified aerogel. Notably, a 2.0 mm-thick sample achieves an NRC value of 0.65, significantly outperforming typical aerogel materials (Fig. 8(d)).

These results can be primarily attributed to the synergistic effects of structural resonance, as well as enhanced viscous and thermal dissipation mechanisms. First, the ultrahigh porosity of the aerogel, combined with the presence of pyrolysis-derived nanoparticles, facilitates multiple internal reflections of incident sound waves. This increases the propagation path length and the frequency of interactions between sound waves and the material interfaces, thereby promoting effective energy dissipation. Second, the aerogel's skeletal framework itself can undergo structural resonance with incident sound waves, further amplifying its sound absorption capability. Finally, the introduction of nanoscale fillers into the aerogel matrix leads to an increased surface roughness, which intensifies the frictional interaction between the material and the incident sound waves. This frictional effect results in additional sound energy being dissipated during wave propagation, further enhancing the acoustic attenuation performance of the aerogel.[74]

Moisture resistance is a crucial factor for the practical application of sound-absorbing materials.[75] To evaluate the moisture resistance and practical application potential of the CS-2 aerogel, we placed the samples in a high-humidity environment (maintained at ~60% relative humidity using a humidifier) and measured their weight at different time intervals to calculate the weight retention rate (Fig. 8(e)). As shown in Fig. 8(f), the sample weight remains stable over time, with no detectable weight change, indicating that the aerogel exhibits excellent moisture resistance and holds significant potential for practical applications.

2.5. Fire resistance performance

To further evaluate the fire safety performance of our synthesized aerogels, we first conducted microscale combustion calorimetry (MCC) tests on both the pristine chitosan aerogel and the BPNS@MOF-modified aerogel prior to carbonization. The results demonstrate that both aerogels exhibit excellent flame retardant properties. Specifically, the pristine chitosan aerogel displayed a peak heat release rate (pHRR) of 61.4 W g^{-1}, while the incorporation of BPNS@MOF further reduced the pHRR to 46.6 W g^{-1}, accompanied by a significant decrease in heat flow (Fig. 9(a) and (b)). This remarkable flame retardant performance can be attributed to the inherent ability of chitosan to rapidly form a protective carbon layer at elevated temperatures, which inhibits flame propagation.[76–78] Moreover, the addition of BPNS@MOF enhances this effect through the catalytic carbonization promoted by the MOF and the barrier effect of black phosphorus, facilitating the formation of a denser char layer and further mitigating combustion risks.

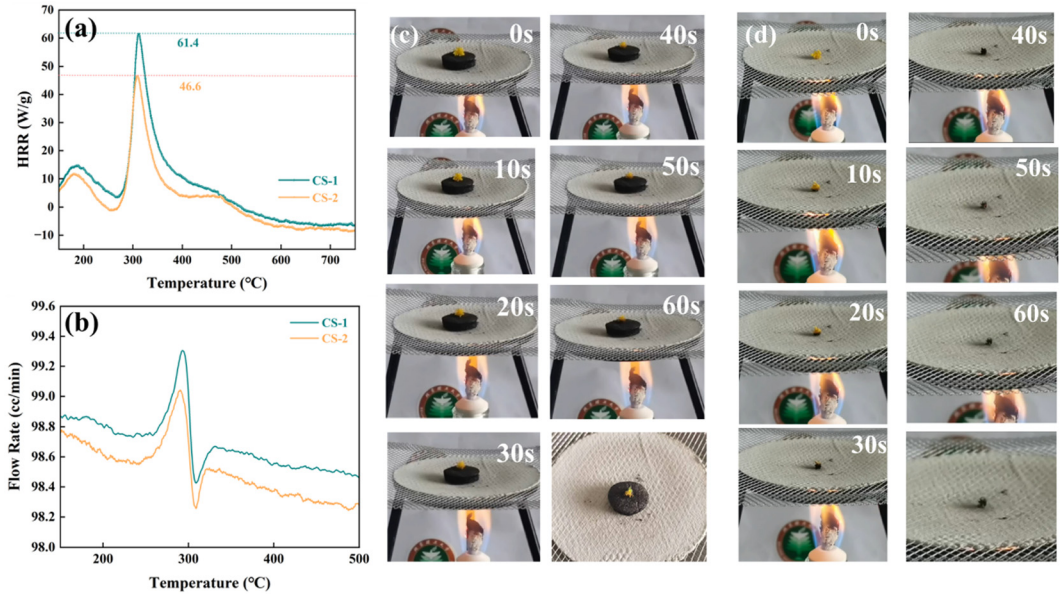

Fig. 9 (a) Heat release rate (HRR) curves and (b) flow rate curves of CS-1 and CS-2; (c) and (d) digital photographs of the ignition tests and the appearance of petals before and after placing them on CS-2 aerogel.

These findings underscore the great potential of these materials for flame retardant applications.[79–81]

To further verify the fire protection capabilities of the carbonized aerogels, we placed fresh flower petals on top of the CS-2 aerogel and exposed the system to a direct flame. Remarkably, after 60 seconds of continuous flame exposure, the CS-2 aerogel showed no obvious degradation, and the petals exhibited only slight shrinkage (Fig. 9(c)). Even when the exposure time was extended to 120 seconds, the petals remained largely intact. In contrast, flower petals without the protective CS-2 aerogel were completely charred within 30 seconds under identical conditions (Fig. 9(d)). These results further confirm the outstanding fire safety potential of the CS-2 aerogel, highlighting its promise for practical fire resistance applications.

3. Conclusions

In summary, we successfully synthesized FeCo-MOF with amine functionalization *via* a hydrothermal method and subsequently assembled it onto the surface of black phosphorus nanosheets through an electrostatic self-assembly strategy. Benefiting from the presence of amino groups on the MOF, BPNS@MOF was effectively grafted onto the chitosan backbone using glutaraldehyde as a crosslinking agent, resulting in the fabrication of chitosan-derived carbon/BPNS@MOF aerogels. The results demonstrate that the incorporation of BPNS@MOF effectively enhances the electromagnetic properties of the chitosan-derived carbon aerogels, achieving outstanding microwave absorption performance. Specifically, the minimum reflection loss (RL_{min}) and the maximum effective absorption bandwidth (EAB) reach −72.13 dB and 5.88 GHz, respectively, over the frequency range of 2.0–18.0 GHz. Mechanistic investigations reveal that excellent attenuation performance arises from the synergistic contributions of conductive loss, magnetic resonance loss, interfacial polarization, dipolar orientation polarization, and multiscale porous architecture. Radar cross-section (RCS) simulations further confirm the material's potential for practical stealth applications. Moreover, the study highlights that the CS-2 aerogel exhibits excellent fire resistance properties and an ultralow thermal conductivity of 0.05 W $(m\ K)^{-1}$, enabling superior infrared stealth capabilities. Additionally, acoustic measurements reveal that even a 5.0 mm-thick sample demonstrates exceptional sound absorption performance, achieving sound absorption coefficients greater than 0.95 in the 2000 Hz and 4500–6500 Hz frequency ranges. These results collectively underscore the remarkable multifunctional potential of the chitosan-derived carbon/BPNS@MOF aerogel, paving the way for its application in advanced electromagnetic wave absorption, thermal insulation, infrared stealth, and noise reduction technologies.

4. Experimental section

All raw materials and most characterization techniques are detailed in the SI.

4.1. Synthesis of FeCo-MOF

First, 2.7 g of ferric chloride hexahydrate and 1.81 g of 2-amino terephthalic acid were accurately weighed and dissolved in an appropriate amount of *N*,*N*-dimethylformamide (DMF) under ultrasonication to enhance solubility. After that, the mixture was put in a stainless steel autoclave lined with Teflon and heated to 150 °C for a full day. Subsequently, 0.698 g of the as-obtained product and 0.506 g of cobalt(II) nitrate hexahydrate were accurately weighed and dispersed in an appropriate amount of DMF. The mixture was stirred vigorously at room temperature for 12 hours, followed by centrifugation, washing with ethanol, and drying to obtain the FeCo-MOF.

4.2. Synthesis of BPNS@MOF

First, a certain amount of black phosphorus was weighed and dispersed in *N*-methylpyrrolidone (NMP). The mixture was subjected to high-energy shear using a cell disruptor for six hours to obtain black phosphorus nanosheets. A total of 0.06 g of black phosphorus nanosheets (BPNSs) were dispersed in an appropriate amount of ethanol. Separately, 0.3 g of FeCo-MOF was dispersed in an appropriate amount of DMF. The two solutions were combined and stirred at room temperature for 24 hours. After centrifugation, washing with ethanol, and drying, the BPNS@MOF composite was obtained.

4.3. Synthesis of CS and CS/BPNS@MOF aerogels

0.01 g of BPNS@MOF and 0.2 g of chitosan were separately dispersed in 20 mL of a 2% (v/v) acetic acid solution under vigorous stirring to form a homogeneous and viscous solution. Subsequently, 1 mL of a 5% (v/v) glutaraldehyde solution was added as a crosslinking agent and stirring was maintained for 2 hours. The resulting solution was poured into molds and freeze-dried for 24 hours to obtain the BPNS@MOF/chitosan aerogel.

4.4. Preparation of carbon aerogels derived from CS and CS/BPNS@MOF

The obtained CS and CS/BPNS@MOF aerogels were placed in a tubular furnace and carbonized under a nitrogen atmosphere. The temperature was increased to 800 °C at a rate of 2 °C per minute, held at this temperature for 2 hours, and then cooled naturally to room temperature. The resulting carbon aerogels were denoted as CS-1 and CS-2, respectively.

Author contributions

Xiuhong Sun: writing – original draft, data curation, methodology, writing – review & editing. Jinhu Hu: methodology, investigation. Jin Cao: methodology, investigation. Lei Chen: data curation. Tinglu Song: data curation, investigation. Xing Su: writing – review & editing, investigation. Pingan Song: supervision, writing – review & editing. Yang Li: writing – review & editing, methodology. Shengchao Huang: writing – review & editing, investigation. Ye-Tang Pan: writing – review & editing, project administration, investigation. Mingliang Ma: investigation, writing – review & editing. Congling Shi: writing – review & editing, methodology.

Conflicts of interest

The authors declare no conflict of interest.

Data availability

All supporting data for this article, including experimental details, additional characterization results and supplementary figures, have been included in the supplementary information associated with this paper. See DOI: **https://doi.org/10.1039/d5mh01066g**

Acknowledgements

The funding for this work was provided by the National Natural Science Foundation of China (no. 22375023), the Natural Science Foundation of Chongqing (CSTB2024NSCQ-MSX0452), the Natural Science Foundation of Hebei Province (E2024105006) and the Natural Science Foundation of Shandong Province (ZR2024ME040).

Notes and references

1 Y. Li, X. Liu, X. Nie, W. Yang, Y. Wang, R. Yu and J. Shui, *Adv. Funct. Mater.*, 2018, **29**, 1807624.
2 J. Ouyang, Z. He, Y. Zhang, H. Yang and Q. Zhao, *ACS Appl. Mater. Interfaces*, 2019, **11**, 39304–39314.
3 J. Liu, H. B. Zhang, X. Xie, R. Yang, Z. Liu, Y. Liu and Z. Z. Yu, *Small*, 2018, **14**, 1802479.
4 P. Liu, C. Zhu, S. Gao, C. Guan, Y. Huang and W. He, *Carbon*, 2020, **163**, 348–359.
5 X. Xu, S. Shi, Y. Tang, G. Wang, M. Zhou, G. Zhao, X. Zhou, S. Lin and F. Meng, *Adv. Sci.*, 2021, **8**, 2002658.
6 N. Qu, G. Xu, Y. Liu, M. He, R. Xing, J. Gu and J. Kong, *Adv. Funct. Mater.*, 2024, **35**, 2402923.
7 W. Gu, A. Xia, C. Jin, H. Zhang, H. Li and G. Ji, *Carbon*, 2024, **229**, 119565.
8 J. Xu, S. Liu, S. Guo, D. Guo, J. Xiang and F. Wen, *Ceram. Int.*, 2024, **50**, 52490–52497.
9 M. Hou, H. Gu, J. Huang, H. Guan and S. Xing, *Synth. Met.*, 2023, **293**, 117251.
10 X. Zhuang, M. Ning, L. Pan, Y. Gao, Q. Zhang, C. Mu, H. Ma, J. Li, G. Tan, Q. Man and B. Shen, *ACS Appl. Electron. Mater.*, 2024, **7**, 601–611.
11 Y. Gao, Z. Lei, L. Pan, Q. Wu, X. Zhuang, G. Tan, M. Ning and Q. Man, *Chem. Eng. J.*, 2023, **457**, 141325.
12 W. Chu, K. Wang, S. Liu, Y. Chen, H. Li and H. Liu, *Mater. Res. Bull.*, 2024, **177**, 112857.
13 N. Chadha and P. Saini, *Mater. Res. Bull.*, 2021, **143**, 111458.
14 J. Xu, *Synth. Met.*, 2023, **295**, 117352.
15 J. Wei, G. Shao and X. Huang, *ACS Appl. Mater. Interfaces*, 2024, **16**, 20969–20979.
16 Z. Zhang, J. Tan, W. Gu, H. Zhao, J. Zheng, B. Zhang and G. Ji, *Chem. Eng. J.*, 2020, **395**, 125190.
17 Y. Tian, D. Estevez, H. Wei, M. Peng, L. Zhou, P. Xu, C. Wu, M. Yan, H. Wang, H.-X. Peng and F. Qin, *Chem. Eng. J.*, 2021, **421**, 129781.
18 F. Chen, S. Zhang, B. Ma, Y. Xiong, H. Luo, Y. Cheng, X. Li, X. Wang and R. Gong, *Chem. Eng. J.*, 2022, **431**, 134007.
19 Q. Sun, X. Zhang, R. Liu, S. Shen, F. Wu and A. Xie, *Nanomaterials*, 2021, **11**, 1164.
20 R. Yuan, J. Lyu, C. Fu, H. Feng and X. Zhang, *ACS Appl. Nano Mater.*, 2023, **6**, 10944–10952.
21 F. Wu, A. Xie, M. Sun, W. Jiang and K. Zhang, *Mater. Lett.*, 2017, **193**, 30–33.
22 M. B. Erande, M. S. Pawar and D. J. Late, *ACS Appl. Mater. Interfaces*, 2016, **8**, 11548–11556.
23 K. Wang, B. M. Szydłowska, G. Wang, X. Zhang, J. J. Wang, J. J. Magan, L. Zhang, J. N. Coleman, J. Wang and W. J. Blau, *ACS Nano*, 2016, **10**, 6923–6932.
24 Z. Wang, Y. Xu, F. Chen, S. Cheng, Z. Yi, G. Xiao, Y. Li, J. Jiang, X. Zhou and Z. Chen, *Optik*, 2022, **270**, 169932.
25 B. Wang, L. Zhang, X. Zhao, J. Xiang, C. Mu, K. Zhai, T. Xue, Z. Liu and F. Wen, *Ceram. Int.*, 2023, **49**, 30837–30844.
26 J. Wang, D. Liu, H. Huang, N. Yang, B. Yu, M. Wen, X. Wang, P. K. Chu and X. F. Yu, *Angew. Chem., Int. Ed.*, 2018, **57**, 2600–2604.
27 J. Luo, L. Wu, J. Yan, X. Lv, Y. Luo, W. Jiang, Z. Xiong, A. Ni, C. Liu and R. Che, *Chin. Chem. Lett.*, 2025, **36**, 111065.
28 X. Zhang, M. Wang, L. Chang, C. Yu, X. Fan, M. Cao and L. Li, *Adv. Funct. Mater.*, 2025, e08333.
29 A. Wang, J. Ni, W. Wang, D. Liu, Q. Zhu, B. Xue, C.-C. Chang, J. Ma and Y. Zhao, *Appl. Catal., B*, 2022, **319**, 121926.
30 K. Ge, S. Sun, Y. Zhao, K. Yang, S. Wang, Z. Zhang, J. Cao, Y. Yang, Y. Zhang, M. Pan and L. Zhu, *Angew. Chem., Int. Ed.*, 2021, **60**, 12097–12102.
31 J. Zhang, C. Mück-Lichtenfeld and A. Studer, *Nature*, 2023, **619**, 506–513.
32 J. Cao, Y.-T. Pan, H. Vahabi, J.-I. Song, P. Song, D.-Y. Wang and R. Yang, *Mater. Today Chem.*, 2024, **37**, 102015.
33 Q. Li, X. Song, Y.-T. Pan, J. Sun, A. Bifulco and R. Yang, *J. Colloid Interface Sci.*, 2024, **674**, 445–458.
34 S. S. M. Ameen, K. M. Omer, F. Shalileh and M. Hosseini, *Mater. Horiz.*, 2025, **12**, 3301–3319.
35 K. Song, X. Bi, D. Wang, Y.-T. Pan, M. Xie, J. He, D.-Y. Wang and R. Yang, *Chem. Eng. J.*, 2024, **495**, 153850.
36 X. Sun, W. Miao, Y. T. Pan, P. Song, S. Gaan, L. H. Ibarra and R. Yang, *Adv. Sustainable Syst.*, 2024, **9**, 2400768.
37 Z. Han, X. Song, Z. Chen, Y.-T. Pan, X. Lai, D.-Y. Wang and R. Yang, *Sustainable Mater. Technol.*, 2024, **41**, e01024.
38 M. Sun, Z. Li, B. Wei, X. Lu, J. Shi, L. Xie, Z. Song, C. Chen, J. Zhong, J. Zhou and F. Wu, *Synth. Met.*, 2023, **292**, 117229.
39 F. Shahbazi Farahani, M. S. Rahmanifar, A. Noori, M. F. El-Kady, N. Hassani, M. Neek-Amal, R. B. Kaner and M. F. Mousavi, *J. Am. Chem. Soc.*, 2022, **144**, 3411–3428.
40 B. Zhao, Y. Li, H. Ji, P. Bai, S. Wang, B. Fan, X. Guo and R. Zhang, *Carbon*, 2021, **176**, 411–420.
41 L. Li, G. Li, W. Ouyang, Y. Zhang, F. Zeng, C. Liu and Z. Lin, *Chem. Eng. J.*, 2021, **420**, 127609.

42 J. Cao, S. Chen, Z. Han, Y.-T. Pan, Y. Lin, W. Wang and R. Yang, *Chem. Eng. J.*, 2024, **501**, 157758.
43 M. Chen, T. Liu, X. Zhang, R. Zhang, S. Tang, Y. Yuan, Z. Xie, Y. Liu, H. Wang, K. V. Fedorovich and N. Wang, *Adv. Funct. Mater.*, 2021, **31**, 2100106.
44 X. Bi, Z. Zhang, K. Song, X. Zhang, Y.-T. Pan, H. Qu, H. Vahabi, J. He and R. Yang, *Composites, Part A*, 2024, **184**, 108283.
45 Q. Peng, W. Yu, C. Gao, L. Geng, P. Fatehi, S. Wang and F. Kong, *Adv. Compos. Hybrid Mater.*, 2025, **8**, 232.
46 Y. Zhao, H. Wang, H. Huang, Q. Xiao, Y. Xu, Z. Guo, H. Xie, J. Shao, Z. Sun, W. Han, X. F. Yu, P. Li and P. K. Chu, *Angew. Chem., Int. Ed.*, 2016, **55**, 5003–5007.
47 D. Liu, R. Qiang, Y. Du, Y. Wang, C. Tian and X. Han, *J. Colloid Interface Sci.*, 2018, **514**, 10–20.
48 K. Song, X. Bi, C. Yu, Y.-T. Pan, H. Vahabi, V. Realinho, J. He and R. Yang, *ACS Appl. Mater. Interfaces*, 2024, **16**, 7617–7630.
49 S. Yin, X. Ren, R. Zheng, Y. Li, J. Zhao, D. Xie and Y. Mei, *Chem. Eng. J.*, 2023, **464**, 142683.
50 K.-L. Zhang, J.-Y. Zhang, Z.-L. Hou, S. Bi and Q.-L. Zhao, *Carbon*, 2019, **141**, 608–617.
51 S. Ren, H. Yu, L. Wang, Z. Huang, T. Lin, Y. Huang, J. Yang, Y. Hong and J. Liu, *Nano-Micro Lett.*, 2022, **14**, 68.
52 X.-X. Wang, T. Ma, J.-C. Shu and M.-S. Cao, *Chem. Eng. J.*, 2018, **332**, 321–330.
53 J. Hu, Z. Jiao, J. Jiang, Y. Hou, X. Su, J. Zhang, C. Feng, Y. Ma, M. Ma and J. Liu, *J. Colloid Interface Sci.*, 2023, **652**, 1825–1835.
54 J. Hu, Y. Liu, J. Jiang, X. Su, C. Feng, Y. Ma, Y. Hou, J. Zhang, Z. Jiao and M. Ma, *Compos. Struct.*, 2023, **312**, 116886.
55 J. Hu, Z. Jiao, X. Han, J. Liu, M. Ma, J. Jiang, Y. Hou, X. Wang, C. Feng and Y. Ma, *J. Mater. Sci. Technol.*, 2024, **175**, 141–152.
56 X. Wang, Y. Yuan, X. Sun, R. Qiang, Y. Xu, Y. Ma, E. Zhang and Y. Li, *Small*, 2024, **20**, 2311657.
57 J. Lin, H. Wen, Z. Feng, R. Hu, L. Wu, C. Liu, S. Lin, Y. Peng, Y. Liu and R. Che, *Adv. Funct. Mater.*, 2025, 2505381.
58 B. Zhang, C. Wu, K. Ye, C. Sun and Z. Wang, *Carbon*, 2023, **213**, 118253.
59 C. Zhang, W. Yang, B. Jiang, Z. Li, S. Du, Z. Ding, X. Wu, W. Zhu, J. Dong, L. Kong, Z. Cao and Y. Li, *Chem. Eng. J.*, 2025, **517**, 164290.
60 Z. Wang, J. Liu, H. Hao, Q. Jing, S. Yan, J. Guo and Z. Wang, *Carbon*, 2024, **217**, 118622.
61 R. Kumar, S. Sahoo and E. Joanni, *Carbon*, 2023, **211**, 118072.
62 Y. Wang, W. Zhang, X. Wu, C. Luo, Q. Wang, J. Li and L. Hu, *Synth. Met.*, 2017, **228**, 18–24.
63 J. Liu, H. Hao, Y. Zhang, L. Wei, Y. Cui, Q. Jing, S. Yan, J. Guo and Z. Wang, *J. Mater. Chem. A*, 2025, **13**, 16061–16069.
64 Y. Jin, J. Zhang, S. Cao, J. Xu, H. Fan, Z. Tabassum, K. Chen and S. Yang, *Compos. Commun.*, 2025, **57**, 102427.
65 S. Zhou, V. Apostolopoulou-Kalkavoura, M. V. Tavares da Costa, L. Bergström, M. Strømme and C. Xu, *Nano-Micro Lett.*, 2019, **12**, 9.
66 D. S. Smith, A. Alzina, J. Bourret, B. Nait-Ali, F. Pennec, N. Tessier-Doyen, K. Otsu, H. Matsubara, P. Elser and U. T. Gonzenbach, *J. Mater. Res.*, 2013, **28**, 2260–2272.
67 X. Li, R. Hu, Z. Xiong, D. Wang, Z. Zhang, C. Liu, X. Zeng, D. Chen, R. Che and X. Nie, *Nano-Micro Lett.*, 2023, **16**, 42.
68 W. Jie, L. Xuening, S. Sisi, W. Zihan, C. Yuting and C. Sheng, *J. Alloys Compd.*, 2024, **1007**, 176299.
69 M. Zhang, S. Jiang, F. Han, M. Li, N. Wang and L. Liu, *Carbohydr. Polym.*, 2021, **264**, 118033.
70 Y. Wang, N. Pang, S. Liu, X. Yin, M. Yu, C. Wang and C. Zhou, *Chem. Eng. J.*, 2024, **498**, 155332.
71 H. Wang, Y. Wang, T. Li, C. Yu, P. Lin, J. Liu, Y. Lan and Y. T. Pan, *Adv. Funct. Mater.*, 2025, 2500800.
72 C. Fan, J. Yang, M. Rui, J. Yang, T. Shi, J. Shen, B. Zhou, C. Liu, J. Zhu and A. Du, *ACS Appl. Mater. Interfaces*, 2025, **17**, 18759–18770.
73 C. Chen, X. Li, P. Yi, Z. Geng, H. Zou, G. Deng, M. Fang, R. Yu, J. Shui and X. Liu, *J. Mater. Sci. Technol.*, 2025, **224**, 80–91.
74 C. Jia, L. Li, Y. Liu, B. Fang, H. Ding, J. Song, Y. Liu, K. Xiang, S. Lin, Z. Li, W. Si, B. Li, X. Sheng, D. Wang, X. Wei and H. Wu, *Nat. Commun.*, 2020, **11**, 3732.
75 W. Guo, S. Chen, F. Liang, L. Jin, C. Ji, P. Zhang and B. Fei, *Int. J. Biol. Macromol.*, 2023, **246**, 125343.
76 K. Song, H. Zhang, Y.-T. Pan, Z. Ur Rehman, J. He, D.-Y. Wang and R. Yang, *J. Colloid Interface Sci.*, 2023, **643**, 489–501.
77 K. Song, X. Li, Y.-T. Pan, B. Hou, Z. U. Rehman, J. He and R. Yang, *Polym. Degrad. Stab.*, 2023, **211**, 110318.
78 K. Song, B. Hou, Z. Ur Rehman, Y.-T. Pan, J. He, D.-Y. Wang and R. Yang, *Chem. Eng. J.*, 2022, **448**, 137666.
79 X. Bi, K. Song, H. Zhang, Y.-T. Pan, J. He, D.-Y. Wang and R. Yang, *Chem. Eng. J.*, 2024, **482**, 148997.
80 X. Bi, K. Song, Z. Zhang, T. Lin, Y. T. Pan, W. Fu, P. Song, J. He and R. Yang, *Small*, 2024, **20**, 2403375.
81 X. Bi, K. Song, Y. T. Pan, C. Barreneche, H. Vahabi, J. He and R. Yang, *Small*, 2023, **20**, 2307492.

